Competing chiral d-wave superconductivity and magnetic phases in the strong-coupling Hubbard model on the honeycomb lattice

F. G. Ribeiro [1,2], E. P. Raposo [1], and M. D. Coutinho-Filho [1]
[1]*Laboratório de Física Teórica e Computacional, Departamento de Física, Universidade Federal de Pernambuco, Recife, Pernambuco 50670-901, Brazil*
[2]*Laboratório de Física, Instituto Federal de Educação, Ciência e Tecnologia da Paraíba, Campus João Pessoa, João Pessoa, Paraíba 58015-435, Brazil*

(Received 1 November 2022; revised 14 February 2023; accepted 15 February 2023; published 23 February 2023)

We address the competing superconducting and magnetic phases on the honeycomb lattice, in a field-theoretic approach suitable to yield a low-energy perturbative theory for the strong-coupling limit of the Hubbard model, both at half filling and in the low and high hole-doped regimes. The effective low-lying Hamiltonian is presented in terms of charge (Grassmann fields) and spin [SU(2) gauge fields] degrees of freedom. We analyze the competing phases by calculating the ground-state energy, electronic spectrum, and other observables associated with the s- and $d_{x^2-y^2}+id_{xy}$-wave superconducting phases, doped antiferromagnetic, and doped ferromagnetic states. We find that, while the antiferromagnetic order has the lowest ground-state energy for low hole doping near half filling, a dominant superconducting state with chiral $d_{x^2-y^2}+id_{xy}$-wave symmetry emerges in the vicinity of the Van Hove singularity in the high hole-doped regime, with the presence of a quantum first-order transition accompanied by spatial phase separation. We highlight that advances in the understanding of chiral superconducting states on the honeycomb lattice are relevant to a number of doped compounds including the graphene monolayer system.

DOI: 10.1103/PhysRevB.107.064510

I. INTRODUCTION

Current research in condensed matter physics has found substantial inspiration in Anderson's pioneering ideas [1,2], particularly those associated with strongly correlated electron systems and the many attempts of explanation of the phenomena related to superconductors exhibiting high critical temperatures (high-T_c superconductivity) [3–6]. From a general viewpoint, one may think of two routes to superconductivity [7]: (i) The electron-phonon BCS theory, based on the assumption that two electrons attract each other when the first polarizes the lattice and the second is drawn to this region; and (ii) the pure electronic coupling, which provides a mechanism for higher superconducting temperatures.

Another topical subject associated with strongly correlated systems is quantum magnetism [8–10], arising due to either itinerant or localized electrons. In the insulating phase, only spin degrees of freedom are relevant, as in the Heisenberg model. In the metallic phase, however, a valid starting point is the Hubbard model, as Anderson invoked shortly after the advent of high-T_c superconductivity [1]. In this context, the spins of the magnetic ions are coupled via the antiferromagnetic (AFM) exchange interaction $J=4t^2/U$, where t is the nearest-neighbor hopping amplitude and U denotes the on-site Coulomb repulsion.

For instance, it has been reported [11–13] that the $In_3Cu_2VO_9$ compound displays an insulating AFM Néel ground state, in which the network of spin-1/2 ($S=1/2$) magnetic Cu^{2+} ($3d^9$) ions on the c plane assumes a honeycomb structure, with the nonmagnetic V^{5+} ions at the centers. As each honeycomb layer is well separated from the others by nonmagnetic In^{3+} ions, this compound can be considered a quasi-two-dimensional (2D) system. Likewise, experimental evidence has been provided [14] that the undoped materials $Na_3T_2SbO_6$, with $T=Cu^{2+}$, $T=Ni^{2+}$ ($3d^9 4s^1$, $S=1$), or $T=Co^{2+}$ ($3d^7$, $S=3/2$), also exhibit AFM order. We also mention that the Ru-Ru bonds in the honeycomb lattice material Li_2RuO_3 present a strong tendency to form local dimers with covalent bonds via direct overlap of the Ru $4d$ orbitals (valence bond crystal) [15].

Other examples are the d-superconducting pnictide SrPtAs [16,17] and vortex configurations in $s+id$ superconductors [18]. The SrPtAs compound displays a hexagonal structure with weakly coupled PtAs layers forming a honeycomb lattice. Interesting physics can be related to the hexagonal arrangement of this material [16,17], e.g., strong spin-orbit coupling at the Pt ions and PtAs layers breaking inversion symmetry. Experimental data have indicated that this compound exhibits a chiral d-wave superconducting state [16,17].

Several theoretical attempts have been made to describe the emergence of superconductivity in the doped graphene monolayer. In particular, it has been shown [19] by means of functional renormalization group (FRG) techniques that in the weak-coupling regime the on-site repulsive Hubbard interaction can lead to a chiral $d_{x^2-y^2}+id_{xy}$-wave superconducting state.

We also remark that the chiral superconducting phase has been reported as well in the strong-coupling limit of the Hubbard model, through either renormalized mean-field theory (RMFT) [20] or the Grassmann tensor product states (GTPS)

approach [21]. We note in [20] that the calculated values of both s- and d-wave pairing parameters are nonzero even for values of the hole-doping density δ above the critical percolation density of the honeycomb lattice. On the other hand, we mention that in [21] the pairing superconducting order parameter has not been evaluated for doping densities higher than $\delta = 0.15$. Recently, we have also [22] applied the Hubbard model in a mean-field approach to address the pseudogap phase in doped cuprate superconductors.

In this work, we apply quantum many-body field-theoretic methods to build a low-energy perturbative theory suitable to describe the superconducting and magnetic properties of the strong-coupling limit of the Hubbard model on the honeycomb lattice, both at half filling (one electron per site on average) and in the low and high hole-doped regimes. In Sec. II, we present, within the framework of a functional-integral approach, the effective low-lying Hamiltonian associated with the charge (Grassmann fields) and spin [SU(2) gauge fields] degrees of freedom. We analyze the competing superconductivity and magnetic phases by calculating the ground-state energy, electronic spectrum, and other observables associated with the s- and $d_{x^2-y^2} + id_{xy}$-wave superconducting phases, doped AFM, and doped ferromagnetic (FM) states.

In Sec. III our results are presented and discussed. We find that, while the AFM order has the lowest ground-state energy for low hole doping near half filling, a dominant superconducting state with chiral $d_{x^2-y^2} + id_{xy}$-wave symmetry emerges in the vicinity of the Van Hove singularity (high hole doping), with the presence of a quantum first-order transition accompanied by spatial phase separation between the doped AFM and chiral superconducting states. Lastly, in Sec. IV we draw some final remarks and conclusions. We also include an Appendix with the calculation of the tight-binding electronic density of states and Van Hove singularity.

II. THEORETICAL BACKGROUND

A. Low-energy effective theory for the half-filled and hole-doped strong-coupling regimes of the Hubbard Hamiltonian on the honeycomb lattice

We start with a brief review of the derivation, in a perturbative functional integral approach, of the low-lying effective Lagrangian and associated Hamiltonian arising from the strong-coupling regime of the half-filled and hole-doped Hubbard Hamiltonian on the honeycomb lattice [23].

The spatial structure of the monolayer honeycomb lattice is depicted in Fig. 1, with the unit cell displaying the sites A and B, which define the respective sublattices [24,25]. We consider N sites and $N_c = N/2$ unit cells labeled $i = 1, \ldots, N_c$, located at positions $\boldsymbol{i}$ on the 2D plane. The associated Hubbard Hamiltonian presents the terms related to the nearest-neighbor electron hopping of amplitude $t > 0$ and on-site Coulomb repulsion of energy $U > 0$ (in $\hbar \equiv 1$ units):

$$\mathcal{H} = -t \sum_{\langle i\alpha, j\beta\rangle\sigma} (\hat{c}^{\dagger}_{i\alpha\sigma}\hat{c}_{j\beta\sigma} + \hat{c}^{\dagger}_{j\beta\sigma}\hat{c}_{i\alpha\sigma}) + U \sum_{i\alpha} \hat{n}_{i\alpha\uparrow}\hat{n}_{i\alpha\downarrow}. \quad (1)$$

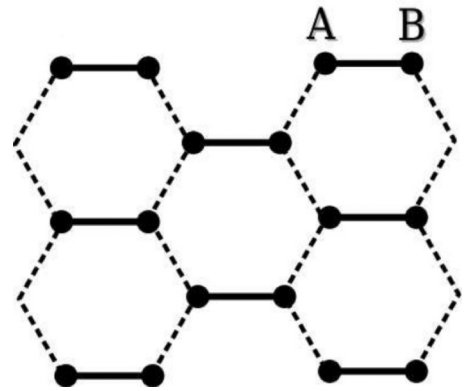

FIG. 1. Honeycomb lattice in real space displaying the two inequivalent A and B sites of a unit cell.

Above $\hat{c}^{\dagger}_{i\alpha\sigma}$ ($\hat{c}_{i\alpha\sigma}$) denotes the creation (annihilation) fermion operator of spin σ ($=\uparrow, \downarrow$) at the site $\alpha = A$ or B of the unit cell i, and $\hat{n}_{i\alpha\sigma} = \hat{c}^{\dagger}_{i\alpha\sigma}\hat{c}_{i\alpha\sigma}$ is the number operator.

The interaction term can be written as

$$\hat{n}_{i\alpha\uparrow}\hat{n}_{i\alpha\downarrow} = \tfrac{1}{2}\hat{\rho}_{i\alpha} - 2(\hat{\boldsymbol{S}}_{i\alpha} \cdot \boldsymbol{n}_{i\alpha})^2, \quad (2)$$

where the standard charge-density and spin-1/2 operators read, respectively,

$$\hat{\rho}_{i\alpha} = \hat{n}_{i\alpha\uparrow} + \hat{n}_{i\alpha\downarrow} \quad (3)$$

and

$$\hat{\boldsymbol{S}}_{i\alpha} = \frac{1}{2}\sum_{\sigma\sigma'} \hat{c}^{\dagger}_{i\alpha\sigma'}\boldsymbol{\sigma}_{\sigma'\sigma}\hat{c}_{i\alpha\sigma}, \quad (4)$$

with $\boldsymbol{\sigma}_{\sigma'\sigma}$ denoting the Pauli matrices, and $\boldsymbol{n}_{i\alpha}$ as a unit vector chosen, without loss of generality, to point along the local spin-quantization axis at each site.

The partition function at temperature $k_B T = \beta^{-1}$ can be built under the usual imaginary-time $\tau \in [0, \beta)$ slicing procedure in the functional integral approach [26–29]. To deal with the anticommuting fermionic operators in Eqs. (1)–(4), a set of Grassmann fields, $\{c^{\dagger}_{i\alpha\sigma}, c_{i\alpha\sigma}\}$, with proper time boundary conditions is introduced at each time slice, associated with a basis $\{|c_{i\alpha\sigma}\rangle\}$ of overcomplete coherent states. A Lagrangian density can be thus obtained with the assignment $\{\hat{c}^{\dagger}_{i\alpha\sigma}, \hat{c}_{i\alpha\sigma}\} \leftrightarrow \{c^{\dagger}_{i\alpha\sigma}, c_{i\alpha\sigma}\}$ between the normally time-ordered creation and annihilation operators and the associated anticommuting Grassmann fields, similarly as done for the sets $\{\hat{\rho}_{i\alpha}, \hat{\boldsymbol{S}}_{i\alpha}\} \leftrightarrow \{\rho_{i\alpha}, \boldsymbol{S}_{i\alpha}\}$.

In the strong-coupling ($U \gg t$) limit at half filling, the ground state of localized spins with long-range AFM order (Néel state) is compatible with the suitable choice [23,30–32]:

$$\boldsymbol{S}_{i\alpha} \cdot \boldsymbol{n}_{i\alpha} = \tfrac{1}{2} p_{i\alpha}\rho_{i\alpha}(2 - \rho_{i\alpha}), \quad (5)$$

where $p_{i\alpha} = \pm 1$ is the staggered factor. Such relation can be properly introduced in the functional integral measure as a weight function in the form of the Gaussian limit of a Dirac delta function. This procedure has the advantage of replacing the quadratic term in Eq. (2) by a linearized form.

In addition, we can also define [23,30–32] a new set of Grassmann fields, $\{a^{\dagger}_{i\alpha\sigma}, a_{i\alpha\sigma}\}$, with spins along the global z axis, from a rotation of the local spin-quantization axis in

the form $a_{i\alpha\sigma} = \sum_{\sigma'}(U_{i\alpha})^{\dagger}_{\sigma\sigma'}c_{i\alpha\sigma'}$, where the SU(2) unitary rotation matrix is generally given by

$$U_{i\alpha} = \begin{bmatrix} \cos\left(\frac{\theta_{i\alpha}}{2}\right) & -\sin\left(\frac{\theta_{i\alpha}}{2}\right)e^{-i\phi_{i\alpha}} \\ \sin\left(\frac{\theta_{i\alpha}}{2}\right)e^{i\phi_{i\alpha}} & \cos\left(\frac{\theta_{i\alpha}}{2}\right) \end{bmatrix}, \quad (6)$$

with $\theta_{i\alpha}$ denoting the polar angle between the z axis and the local unit vector $\boldsymbol{n}_{i\alpha}$, and $\phi_{i\alpha}$ as an arbitrary azimuthal angle due to the U(1) gauge freedom.

With all these ingredients in hand, the Lagrangian density $\mathcal{L} = \mathcal{L}_0 + \mathcal{L}_n$ displays a term $\mathcal{L}_0$ with only charge degrees of freedom (Grassmann fields $\{a^{\dagger}_{i\alpha\sigma}, a_{i\alpha\sigma}\}$), and a term $\mathcal{L}_n$ that couples charge and spin [SU(2) gauge fields $\{U^{\dagger}_{i\alpha}, U_{i\alpha}\}$]. Interestingly, the Hamiltonian $\mathcal{H}_0$ associated with $\mathcal{L}_0$ can be exactly diagonalized in momentum space as a function of the Bogoliubov fields, $\{\alpha^{\dagger}_{\boldsymbol{k}\sigma}, \alpha_{\boldsymbol{k}\sigma}\}$ and $\{\beta^{\dagger}_{\boldsymbol{k}\sigma}, \beta_{\boldsymbol{k}\sigma}\}$, through the transformation [23]

$$a_{i\alpha\sigma} = \frac{1}{\sqrt{N_c}}\sum_{\boldsymbol{k}\sigma} e^{i\boldsymbol{k}\cdot\boldsymbol{i}}[(u_{\boldsymbol{k}} + \sigma v_{\boldsymbol{k}})\alpha_{\boldsymbol{k}\sigma} + (u_{\boldsymbol{k}} - \sigma v_{\boldsymbol{k}})\beta_{\boldsymbol{k}\sigma}], \quad (7)$$

where $u_{\boldsymbol{k}}$ and $v_{\boldsymbol{k}}$ are auxiliary functions with the signature of the honeycomb lattice and $\boldsymbol{k}$ are vectors in the first Brillouin zone. The diagonalized Hamiltonian $\mathcal{H}_0$ presents two dispersive energy bands separated by a Hubbard energy gap U, with the lower-α (upper-β) band associated with the set $\{\alpha^{\dagger}_{\boldsymbol{k}}, \alpha_{\boldsymbol{k}}\}$ ($\{\beta^{\dagger}_{\boldsymbol{k}}, \beta_{\boldsymbol{k}}\}$). We also mention that in the noninteracting tight-binding case ($U = 0$) the bands intersect at the so-called Dirac points [33].

Here we are concerned with the low-energy regime, in which case $J \equiv 4t^2/U \ll 1$. So, by expanding the full Hamiltonian $\mathcal{H} = \mathcal{H}_0 + \mathcal{H}_n$ up to order $O(J)$, and considering that the associated upper-β energy band remains unoccupied in the half-filled and hole-doped strong-coupling regimes (high energy cost for double site occupancy), we finally obtain the effective low-lying Hamiltonian in the hole representation for the honeycomb lattice [23]:

$$\begin{aligned}\mathcal{H} = &-\mu\sum_{\boldsymbol{i}}(1 - h^{\dagger}_{\boldsymbol{i}}h_{\boldsymbol{i}}) \\ &- \sum_{\boldsymbol{i}\alpha\sigma}\theta(\sigma)(U^{\dagger}_{\boldsymbol{i}\alpha}\partial_{\tau}U_{\boldsymbol{i}\alpha})_{\sigma\sigma}(1 - h^{\dagger}_{\boldsymbol{i}}h_{\boldsymbol{i}}) \\ &- t\sum_{\boldsymbol{i}j\alpha\beta\sigma}\left[\theta(\sigma)\left(U^{\dagger}_{\boldsymbol{i}\alpha}U_{\boldsymbol{i}+\hat{\boldsymbol{e}}_j\beta}\right)_{\sigma,-\sigma}h\boldsymbol{i}^{\dagger}h_{\boldsymbol{i}+\hat{\boldsymbol{e}}_j} + \text{H.c.}\right] \\ &+ \frac{J}{8t}\sum_{\boldsymbol{i}j\alpha\sigma}(U^{\dagger}_{\boldsymbol{i}\alpha}\partial_{\tau}U_{\boldsymbol{i}\alpha})_{\sigma,-\sigma}\left[\theta(\sigma)h^{\dagger}_{\boldsymbol{i}}\left(h_{\boldsymbol{i}+\hat{\boldsymbol{e}}_j} + h_{\boldsymbol{i}-\hat{\boldsymbol{e}}_j}\right)\right. \\ &\left. + \text{H.c.}\right] - \frac{J}{8}\sum_{\boldsymbol{i}j\alpha\beta\sigma}\theta(\sigma)\left[\left|\left(U^{\dagger}_{\boldsymbol{i}\alpha}U_{\boldsymbol{i}+\hat{\boldsymbol{e}}_j\beta}\right)_{\sigma\sigma}\right|^2\right. \\ &\left. + \left|\left(U^{\dagger}_{\boldsymbol{i}\alpha}U_{\boldsymbol{i}-\hat{\boldsymbol{e}}_j\beta}\right)_{\sigma\sigma}\right|^2\right](1 - h^{\dagger}_{\boldsymbol{i}}h_{\boldsymbol{i}}), \end{aligned} \quad (8)$$

where μ denotes the chemical potential ($\mu = 0$ at half filling), $\theta(\sigma)$ is the Heaviside step function, with $\theta(\sigma)\theta(-\sigma') = \theta(\sigma)\delta_{\sigma,-\sigma'}$, $\hat{\boldsymbol{e}}_j$ represents the unit vectors along the directions linking the nearest-neighbor sites on the honeycomb lattice, $\{\hat{\boldsymbol{e}}_1 = (1, 0);\ \hat{\boldsymbol{e}}_2 = (-1/2, \sqrt{3}/2);\ \hat{\boldsymbol{e}}_3 = (-1/2, -\sqrt{3}/2)\}$ (see Fig. 1), and the spinless fields for holes in the lower-α band (i.e., holes in the half-filled Néel state) are such that $h^{\dagger}_{\boldsymbol{i}}h_{\boldsymbol{i}} = 1 - \alpha^{\dagger}_{\boldsymbol{i}}\alpha_{\boldsymbol{i}}$.

To end this subsection, we note that the identity

$$\left|\left(U^{\dagger}_{\boldsymbol{i}\alpha}U_{\boldsymbol{i}+\hat{\boldsymbol{e}}_j\beta}\right)_{\sigma\sigma}\right|^2 = \tfrac{1}{2}\left(1 + \boldsymbol{n}_{\boldsymbol{i}\alpha}\cdot\boldsymbol{n}_{\boldsymbol{i}+\hat{\boldsymbol{e}}_j\beta}\right) \quad (9)$$

turns Eq. (8) in the strong-coupling low-doped regime into the t-J Hamiltonian, with AFM exchange coupling J between nearest-neighbor spins [23,34,35]. Moreover, in the strong-coupling limit at half filling, Eq. (8) gives rise to the Heisenberg Hamiltonian with fully localized spins at sites A and B (Néel ground state with long-range AFM order) of the honeycomb lattice [23], as expected.

B. Competing superconductivity and magnetic phases

Hamiltonian (8) can be generally used to describe the electronic spectrum and thermodynamics of the honeycomb lattice with competing superconducting and magnetic orderings. Indeed, we shall see that, while the AFM order has the lowest ground-state energy for low hole doping near half filling, a dominant superconducting state with chiral $d_{x^2-y^2} + id_{xy}$-wave symmetry emerges in the vicinity of the Van Hove singularity (high hole doping), with occurrence of a quantum first-order transition accompanied by spatial phase separation.

1. Superconducting symmetries

The superconducting (SC) states with spin-singlet s-, $d_{x^2-y^2}$- and d_{xy}-wave pairing symmetries on the honeycomb lattice [19,20,36–40] can be accessed by considering SU(2) gauge fields, Eq. (6), with the proper parametrization [41],

$$U^{\text{SC}}_{i\alpha} = \begin{bmatrix} \sum_j \chi_{\hat{\boldsymbol{e}}_j} & -\sum_j \Delta_{\hat{\boldsymbol{e}}_j} \\ \sum_j \Delta_{\hat{\boldsymbol{e}}_j} & \sum_j \chi_{\hat{\boldsymbol{e}}_j} \end{bmatrix}, \quad (10)$$

where $\Delta_{\hat{\boldsymbol{e}}_j}$ and $\chi_{\hat{\boldsymbol{e}}_j}$ are, respectively, the nearest-neighbor spin-singlet pairing and single-particle hopping correlations on the basis $\{\hat{\boldsymbol{e}}_j\} = \{\hat{\boldsymbol{e}}_1, \hat{\boldsymbol{e}}_2, \hat{\boldsymbol{e}}_3\}$. Actually, by writing Eq. (6) in the form of Eq. (10), we can obtain the diagonal Hamiltonian in the convenient Nambu spinor representation, $\Psi_{\boldsymbol{k}} = (\alpha_{\boldsymbol{k}}\ \ \beta_{\boldsymbol{k}})^{\text{T}}$:

$$\mathcal{H}_{SC} = \sum_{\boldsymbol{k}}\Psi^{\dagger}_{\boldsymbol{k}}\tilde{E}^{SC}_{\boldsymbol{k}}\Psi_{\boldsymbol{k}} + \frac{3JN_c\chi^2}{2} + \sum_j\frac{JN_c\Delta^2_{\hat{\boldsymbol{e}}_j}}{2} - N_c\mu, \quad (11)$$

with the two-band spectrum of the superconducting phases described by the 2×2 matrix, $\tilde{E}^{SC}_{\boldsymbol{k}} = (-1)^i E^{SC}_{\boldsymbol{k}}\delta_{ij}$, with

$$E^{SC}_{\boldsymbol{k}} = \left\{\left[\epsilon_{\boldsymbol{k}}\chi_{\boldsymbol{k}}\Delta_{\boldsymbol{k}} + \frac{J}{4t^2}(\chi_{\boldsymbol{k}}\epsilon_{\boldsymbol{k}})^2 - \frac{\mu}{2} + \frac{J}{4t^2}\chi_{\boldsymbol{k}}\Delta_{\boldsymbol{k}}\epsilon^2_{\boldsymbol{k}}\right]^2 + (\epsilon_{\boldsymbol{k}}\chi_{\boldsymbol{k}}\Delta_{\boldsymbol{k}})^2\right\}^{1/2}, \quad (12)$$

where $\Delta_{\boldsymbol{k}}$ and $\chi_{\boldsymbol{k}}$ are the Fourier transforms of $\Delta_{\hat{\boldsymbol{e}}_j}$ and $\chi_{\hat{\boldsymbol{e}}_j}$, respectively, and

$$\epsilon_{\boldsymbol{k}} = t\sqrt{3 + 2\cos(\sqrt{3}k_y) + 4\cos\left(\frac{3k_x}{2}\right)\cos\left(\frac{\sqrt{3}k_y}{2}\right)}. \quad (13)$$

In addition, the symmetry analysis of the pairing component Δ of the superconducting order parameter on the

honeycomb lattice gives rise [36–40] to the following representation on the basis $\{\hat{\boldsymbol{e}}_j\}$ for each associated symmetry state:

$$\Delta_{\hat{\boldsymbol{e}}_j} = \begin{cases} \Delta(1,1,1), & s\text{-wave state;} \\ \Delta(2,-1,-1), & d_{x^2-y^2}\text{-wave state;} \\ \Delta(0,1,-1), & d_{xy}\text{-wave state.} \end{cases} \tag{14}$$

The Fourier transform $\Delta_{\boldsymbol{k}}$ highlights the differences between the above symmetries, as, for example, in the low wave-vector expansion, $|\boldsymbol{q}| = |\boldsymbol{K}_{\pm} + \boldsymbol{k}| \ll 1$, around the Dirac points (i.e., near the top energy states of the lower band), $K_{\pm} = (2\pi/3, \pm 2\pi/3\sqrt{3})$, which implies (for unit lattice constant, $a \equiv 1$)

$$\Delta_{\boldsymbol{q}} \approx \begin{cases} \pm 3\Delta|\boldsymbol{k}|/2, & s\text{-wave state;} \\ -\Delta\left(k_x^2 - k_y^2\right)/|\boldsymbol{k}|^2, & d_{x^2-y^2}\text{-wave state;} \\ \pm\Delta\, k_x k_y/\sqrt{3}|\boldsymbol{k}|^2, & d_{xy}\text{-wave state.} \end{cases} \tag{15}$$

We now turn to the thermodynamic analysis of the above superconducting states. We first write the Nambu fields in terms of the fermionic Matsubara frequencies [26], $\omega_n = (2n+1)\pi/\beta$, with n integer:

$$\Psi_{\boldsymbol{k}} = \frac{1}{\sqrt{\beta}} \sum_n \Psi_{\boldsymbol{k}n} e^{-i\omega_n \tau}. \tag{16}$$

The Legendre transform of $\mathcal{H}_{SC}$, Eq. (11), yields the associated Lagrangian and effective action,

$$\mathcal{S}_{SC} = \sum_{\boldsymbol{k}n} \Psi^{\dagger}_{\boldsymbol{k}n}\left(-i\omega_n + \tilde{E}^{SC}_{\boldsymbol{k}}\right)\Psi_{\boldsymbol{k}n} + \frac{JN_c\beta}{2}\sum_j \Delta^2_{\hat{\boldsymbol{e}}_j} + \frac{3JN_c\beta\chi^2}{2} - \beta\mu N_c. \tag{17}$$

From the saddle point procedure, we obtain the free energy:

$$\mathcal{F}_{SC} = -\sum_{\vec{k}} \oint \frac{dz}{2i\pi} f(z) \ln\left[z^2 - E^2_{\boldsymbol{k}}\right] + \frac{JN_c}{2}\sum_j \Delta^2_{\hat{\boldsymbol{e}}_j} + \frac{3JN_c\chi^2}{2} - N_c\mu, \tag{18}$$

in which the Matsubara sum has been converted [29] into a contour integral performed anticlockwise around the poles $z_{\pm} = \pm E^{SC}_{\boldsymbol{k}}$. The resulting expression for $\mathcal{F}_{SC}$ is then minimized with respect to Δ and χ for the superconducting state symmetries displayed in Eq. (14). In addition, we also define the doping density for holes in the α band, $\delta = 1 - n$, so that the average electron density $n = 1$ at half filling ($\delta = 0$), with $n = N_c^{-1}(\partial\mathcal{F}_{SC}/\partial\mu)_{\Delta,\chi}$. These considerations lead to a system of self-consistent equations for Δ, χ, and μ, as functions of the temperature T, coupling J, and hole doping δ.

For instance, we obtain in the case of the s-wave state the following system:

$$\Delta_s = \frac{2}{3JN_c}\sum_{\boldsymbol{k}} \tanh\left(\frac{E^{SC,s}_{\boldsymbol{k}}}{2k_BT}\right)\frac{\partial E^{SC,s}_{\boldsymbol{k}}}{\partial\Delta_s}, \tag{19}$$

$$\chi_s = \frac{2}{3JN_c}\sum_{\boldsymbol{k}} \tanh\left(\frac{E^{SC,s}_{\boldsymbol{k}}}{2k_BT}\right)\frac{\partial E^{SC,s}_{\boldsymbol{k}}}{\partial\chi_s}, \tag{20}$$

$$\delta_s = -\frac{1}{N_c}\sum_{\boldsymbol{k}} \tanh\left(\frac{E^{SC,s}_{\boldsymbol{k}}}{2k_BT}\right)\frac{\partial E^{SC,s}_{\boldsymbol{k}}}{\partial\mu}. \tag{21}$$

It is important to notice above that $\Delta_s^2 + \chi_s^2 = 1/3$, due to the unitarity condition (unit determinant) of the SU(2) matrix $U^{SC}_{i\alpha}$, Eq. (10). By taking the limit $T \to 0$ and replacing the discrete sums by momentum integrals in the first Brillouin zone (BZ), the ground-state energy per site for the s-wave pairing symmetry reads

$$\frac{E_s}{N} = \frac{t}{4\pi^2}\int_{\mathrm{BZ}} d^2\boldsymbol{k} E^{SC,s}_{\boldsymbol{k}} + \frac{3J}{4}(\Delta^2 + \chi^2). \tag{22}$$

A similar procedure can be also applied to study the chiral $d_{x^2-y^2} + id_{xy}$ ($\equiv d_1 + id_2$) pairing symmetry suggested for the superconducting state on the honeycomb lattice [19,20,36–40]. In this case, we find the system of equations

$$\Delta_{d_1+id_2} = \frac{1}{4JN_c}\sum_{\boldsymbol{k}} \tanh\left(\frac{E^{SC,d_1+id_2}_{\boldsymbol{k}}}{2k_BT}\right)\frac{\partial E^{SC,d_1+id_2}_{\boldsymbol{k}}}{\partial\Delta_{d_1+id_2}}, \tag{23}$$

$$\chi_{d_1+id_2} = \frac{2}{3JN_c}\sum_{\boldsymbol{k}} \tanh\left(\frac{E^{SC,d_1+id_2}_{\boldsymbol{k}}}{2k_BT}\right)\frac{\partial E^{SC,d_1+id_2}_{\boldsymbol{k}}}{\partial\chi_{d_1+id_2}}, \tag{24}$$

$$\delta_{d_1+id_2} = -\frac{1}{N_c}\sum_{\boldsymbol{k}} \tanh\left(\frac{E^{SC,d_1+id_2}_{\boldsymbol{k}}}{2k_BT}\right)\frac{\partial E^{SC,d_1+id_2}_{\boldsymbol{k}}}{\partial\mu}, \tag{25}$$

with the unitarity condition $8\Delta^2_{d_1+id_2} + 3\chi^2_{d_1+id_2} = 1$. The ground-state energy per site for the chiral $d_1 + id_2$-wave pairing is then given by

$$\frac{E_{d_1+id_2}}{N} = \frac{t}{4\pi^2}\int_{\mathrm{BZ}} d^2\boldsymbol{k} E^{SC,d_1+id_2}_{\boldsymbol{k}} + 2J\Delta^2 + \frac{3J}{4}\chi^2. \tag{26}$$

Figures 2(a) and 2(b) present, respectively, the pairing Δ and hopping χ components of the superconducting order parameter as a function of the hole doping δ, for the chiral $d_1 + id_2$-wave superconducting state with $J/t = 1/3$ (i.e., $U/t = 12$) and $T = 0$. We notice in Fig. 2(a) that the onset of the chiral $d_1 + id_2$-wave state takes place around $\delta \approx 0$, with the optimal doping occurring at $\delta_{\mathrm{opt}} \approx 0.15$. Further, we also observe that, beyond the critical hole density $\delta_c \approx 0.39$, the chiral $d_1 + id_2$-wave superconducting phase disappears as the pairing component Δ nullifies. This value is close to the critical percolation density of the honeycomb lattice [42], $\rho_c = 0.42 \pm 0.01$. In fact, the hole density $\delta = 0.42$ is indicated by the right open circles in Figs. 2(a) and 2(b).

On the other hand, Fig. 2(b) shows that the hopping component χ is nonzero everywhere, with a minimum at $\delta_{\mathrm{opt}} \approx 0.15$. We remark, however, that the strong-coupled half-filled system is an insulator at $\delta = 0$ (Néel AFM order with localized spins). In this case, from the unitarity condition with $\Delta = 0$ we find $\chi = 1/\sqrt{3} \approx 0.577$ [left open circle in Fig. 2(b)]. This result is in very good agreement with the maximum value (≈ 0.576) obtained for the tight-binding hopping correlation [23]. We also find $\chi = 1/\sqrt{3}$ at the critical hole doping $\delta = \delta_c$. This fact suggests that, in the high hole-doped regime with $\delta > \delta_c$, the system is essentially governed by the Hamiltonian $\mathcal{H}_0$ with only charge degrees of freedom.

The behavior of the hopping component χ is intrinsically related to the superconducting pairing formation mechanism, which in the present work is governed by purely electronic interactions. From the phenomenological viewpoint, the spin-singlet pairing correlations acquire their maximum absolute value around the so-called M points (see below), so that one

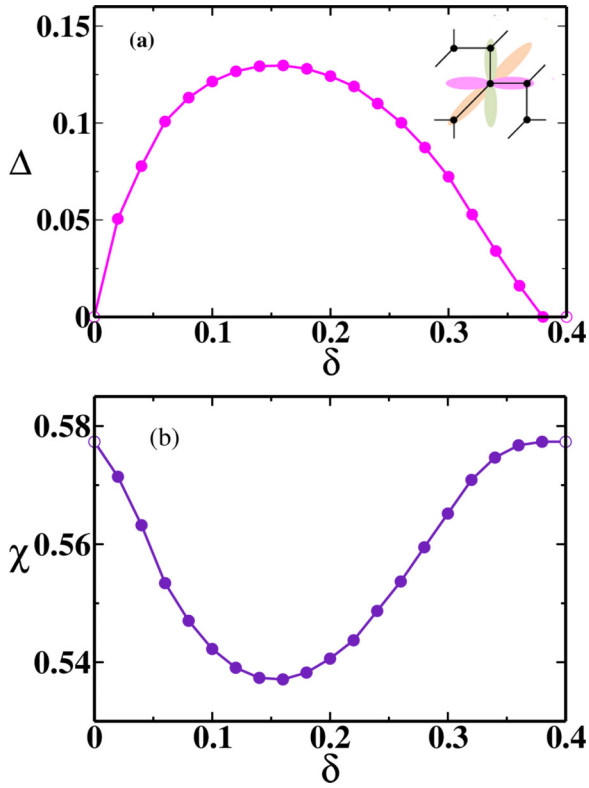

FIG. 2. (a) Pairing Δ and (b) hopping χ components of the superconducting order parameter for $J/t = 1/3$ and $T = 0$, as a function of the hole-doping density δ for the chiral $d_1 + id_2$-wave state. At the optimal doping, $\delta_{\rm opt} \approx 0.15$, Δ is maximum and χ is minimum. The chiral superconducting phase disappears at the critical hole density, $\delta_c \approx 0.39$, where Δ nullifies. Inset of (a): Illustration of the chiral $d_1 + id_2$-wave state taken from [43].

can realize the formation of the superconducting state. Thus, as a consequence of the onset of the superconducting phase, the mean value of the single-particle hopping correlations should present a small and smooth decrease. The way this decrease takes place is governed by the SU(2) constraint employed in our mathematical description of the superconducting phase [unitarity of the SU(2) matrix U (gauge fields)].

From the saddle-point free energy $\mathcal{F}_{SC}$, Eq. (18), we can also determine the superconducting critical temperature T_c for both s- and chiral $d_1 + id_2$-wave state symmetries. We first minimize $\mathcal{F}_{SC}$ with respect to Δ in the $\Delta \to 0$ limit, along with the closed gap condition from Eq. (12), $(J/4t^2)(\chi_k \epsilon_k)^2 - \mu/2 = 0$. In the vicinity of the critical point of the first BZ [M point with wave vector $(2\pi/3, 0)$], the density of states is logarithmically divergent (Van Hove singularity) [19,44] (see Appendix). In this case, by rearranging terms conveniently we obtain

$$\frac{8\pi^2 t^2}{9U^2} = \sum_{n=0}^{\infty} \left[\frac{1}{n + \frac{1}{2}} - \frac{1}{n + \frac{1}{2} + J(2\pi k_B T_c \Gamma)^{-1}} \right], \quad (27)$$

where $\Gamma = \sum_j \cos(\boldsymbol{k} \cdot \hat{\boldsymbol{e}}_j)$ is the form factor for each superconducting state symmetry evaluated at the M point. By writing the sum in n in terms of the digamma function $\psi(z)$ [45], and using that $\psi(z) \approx \ln z$, we find that the critical temperatures $T_{c,\gamma}$, for the $\gamma = s$ and $\gamma = d_1 + id_2$ symmetries, assume the form

$$k_B T_{c,\gamma} = \left[\frac{e^{-\psi(\frac{1}{2})}}{2\pi} \right] \frac{J}{\Gamma_\gamma} e^{-\frac{8\pi^2 t^2}{9U^2}}. \quad (28)$$

The direct proportionality of T_c with the coupling $J = 4t^2/U$ suggests a superconductivity scenario in both s-wave and chiral $d_1 + id_2$-wave states based on a dominant electronic mechanism.

2. *Magnetic states: Antiferromagnetism and ferromagnetism*

Suitable choices for the SU(2) matrix of gauge fields, Eq. (6), also allow the description of phases with AFM and FM orderings.

In the AFM case, with nearest-neighbor spins at sites A and B of the honeycomb lattice pointing antiparallel, we consider $\theta_{iA} = \theta_{iB} = 0$ and $\phi_{iA} = \phi_{iB} = 0$ in Eq. (6) (recall that we are using a staggered representation of spins). From Eq. (3) the average occupancies of these sites read

$$\langle \rho_{iA} \rangle = \frac{n}{2} + \frac{\langle m_{iA} \rangle}{2}, \quad \langle \rho_{iB} \rangle = \frac{n}{2} - \frac{\langle m_{iB} \rangle}{2}, \quad (29)$$

where $\langle m_{iA} \rangle = -\langle m_{iB} \rangle = m$ denotes the sublattice magnetization. A procedure similar to the one described above yields the saddle-point free energy of the AFM phase:

$$\mathcal{F}_{\rm AFM} = -2k_B T \sum_{\boldsymbol{k}} \ln \left[2 \cosh \left(\frac{E_{\boldsymbol{k}}^{\rm AFM}}{2k_B T} \right) \right] + \frac{JN_c}{4}(1 + m^2) - N_c \mu, \quad (30)$$

with the two-band spectrum of energies $\pm E_{\boldsymbol{k}}^{\rm AFM}$, where

$$E_{\boldsymbol{k}}^{\rm AFM} = \left\{ [\epsilon_{\boldsymbol{k}}(1+m)]^2 + \left[\frac{J(1+m^2)}{8} + \frac{\mu}{2} - \frac{J(1-m^2)\epsilon_{\boldsymbol{k}}}{8t} \sum_j \cos\left(2\boldsymbol{k} \cdot \hat{\boldsymbol{e}}_j\right) \right]^2 \right\}^{1/2}. \quad (31)$$

Minimization of $\mathcal{F}_{\rm AFM}$ with respect to m and the calculation of δ from the derivative of $\mathcal{F}_{\rm AFM}$ with respect to μ give rise to a set of self-consistent equations for m and δ, which allow us to obtain the ground-state energy per site of the AFM phase:

$$\frac{E_{\rm AFM}}{N} = \frac{t}{4\pi^2} \int_{\rm BZ} d^2\boldsymbol{k} E_{\boldsymbol{k}}^{\rm AFM} + \frac{J}{4}(1 + m^2). \quad (32)$$

An analogous approach can be also applied to the case with FM order, in which $\theta_{iA} = 0$, $\theta_{iB} = \pi$, and $\phi_{iA} = \phi_{iB} = 0$, where $\langle \rho_{i\alpha} \rangle = (n + \langle m_{i\alpha} \rangle)/2$ and $\langle m_{i\alpha} \rangle = m$, for $\alpha = A, B$. The expression for the FM ground-state energy per site has the same form of Eq. (32), i.e.,

$$\frac{E_{FM}}{N} = \frac{t}{4\pi^2} \int_{\rm BZ} d^2\boldsymbol{k} E_{\boldsymbol{k}}^{FM} + \frac{J}{4}(1 + m^2), \quad (33)$$

but with the FM electronic spectrum $E_{\boldsymbol{k}}^{FM}$ displaying $(1 + m^2)$, instead of $(1 - m^2)$, in the prefactor of the cosine term in Eq. (31).

III. RESULTS AND DISCUSSION

We can now compare the ground-state energies of the superconducting s- and chiral $d_1 + id_2$-wave states, AFM, and FM phases, respectively given in Eqs. (22), (26), (32), and (33), as functions of the normalized coupling J/t and hole-doping density δ.

It is important to remark that the full computation of these ground-state energies involves, first, the numerical solution of the self-consistent equations for the associated observables [e.g., Eqs. (23)–(25) in the $T \to 0$ limit for the superconducting chiral $d_1 + id_2$-wave state symmetry]. Hence, the respective electronic spectrum is determined [Eq. (12) in this case]. Lastly, the ground-state energy is obtained by performing the integration of the electronic spectrum over the first BZ, as in Eq. (26) for the chiral symmetry.

We first notice that the consistency and reliability of our approach has already been confirmed in our previous work [23], which focused specifically on the magnetic properties of the strongly coupled doped Hubbard model on the honeycomb lattice under the very same approach. We start by reviewing some of these previous results obtained from a variety of techniques. For example, our finding [23] for the ground-state energy, $E_0/(NJ) = -0.5489$, in the strong-coupled half-filled regime compares nicely with the values $E_0/(NJ) = -0.5440$ (quantum Monte Carlo (QMC) simulations [46,47]), $E_0/(NJ) = -0.5489$ (second-order spin-wave analysis [48]), $E_0/(NJ) = -0.5443$ (series expansion [49]), $E_0/(NJ) = -0.5445$ (TPS [50–52]), and $E_0/(NJ) = -0.5441$ (GTPS [21]). On the other hand, our result for the staggered magnetization per site in this regime reads [23] $m = 0.2418$, which is also in good agreement with $m = 0.22 \pm 0.03$ (QMC [46]), $m = 0.2681(8)$ (QMC [47]), $m = 0.2418$ (second-order spin-wave analysis [48]), $m = 0.266(9)$ (series expansion [49]), $m = 0.2142$ for virtual dimension $D = 8$ (TPS [50,51]), and $m = 0.285$ for $D \to \infty$ (TPS [52]), while simulations using GTPS [21] yield somewhat larger values: $m = 0.3257$ for $D = 10$ and $m = 0.3239$ for $D = 12$. Likewise, in the doped regime with $\delta < 0.1$ and for $t/J = 3$, our results for $E_0/(NJ)$ and m also compare well with those from QMC simulations [46] and GTPS calculations [21] (see, e.g., Figs. 3 and 4 of our work [23], though with some difference to the GTPS results for m in $D = 12$ [21]).

In the present work, we begin our analysis in the low hole-doped regime. Figure 3 presents the ground-state energy per site as a function of J/t, for the chemical potential $\mu/t = -0.2$ corresponding to small hole concentrations near half filling, with the hole density δ well below the critical hole doping δ_c. We observe that the lowest ground-state energy for any J/t in the displayed interval is that of the doped AFM phase (blue squares). Interestingly, the superconducting chiral $d_1 + id_2$-wave state (pink circles) is the one presenting the highest energy at $T = 0$, monotonically followed by the s-wave state (green triangles up), and doped FM (brown triangles down) orderings. Clearly, this sequence is remnant of the long-range AFM Néel state with localized spins, characteristic of the $J/t \ll 1$ ($U \gg t$) strong-coupling regime at half filling ($\mu = 0$, $n = 1$, $\delta = 0$). In the low-doped AFM scenario, a small concentration of holes in the Néel state removes electrons from the top energy states of the lower $-E_{\boldsymbol{k}}^{\mathrm{AFM}}$ band

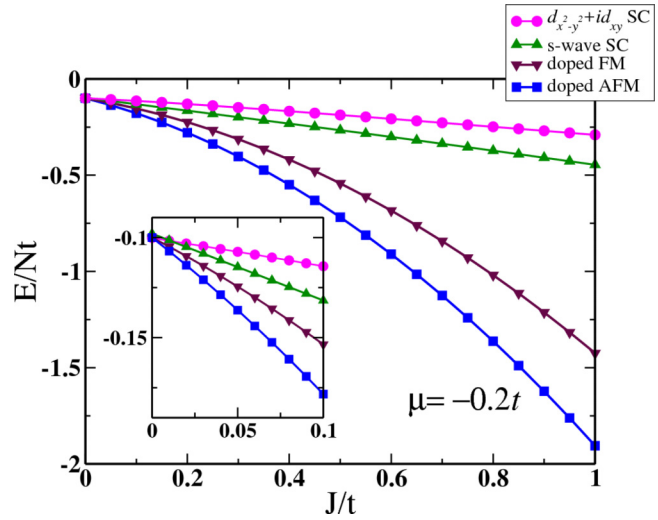

FIG. 3. Ground-state energy per site (in t units), $E/(Nt)$, as a function of the normalized coupling J/t, for the chemical potential $\mu/t = -0.2$ in the low-doped regime of small hole concentrations. Symbols and colors indicate the states: doped AFM, doped FM, and superconducting with s- and chiral $d_1 + id_2$-wave state symmetries. In the low-doped regime near half filling, the lowest (highest) ground-state energy corresponds to that of the doped AFM (superconducting chiral) state, as depicted by blue squares (pink circles). Inset: Detail of the strong-coupling $J/t \ll 1$ region, featuring the degenerate $J/t = 0$ (infinite-U) limit.

in the AFM electronic spectrum (i.e., near the Dirac points), Eq. (31). In this regime, the spatial AFM arrangement of spins still remains considerably undisturbed, differently from the high-doped picture analyzed as follows.

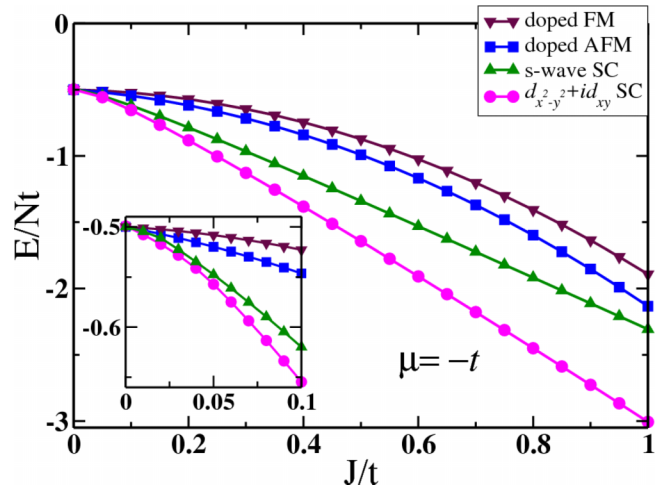

FIG. 4. Ground-state energy per site (in t units), $E/(Nt)$, as a function of the normalized coupling J/t, for the chemical potential $\mu/t = -1$ in the high-doped regime near the critical hole density δ_c (Van Hove singularity). Symbols and colors as in Fig. 3. In the high-doped regime away from half filling, the lowest ground-state energy corresponds to that of the superconducting chiral $d_1 + id_2$-wave state (pink circles). Inset: Detail of the strong-coupling $J/t \ll 1$ region, featuring the degenerate $J/t = 0$ (infinite-U) limit.

The fact that in Fig. 3 the FM state is the second energetically favorable order is somewhat surprising, since one is still far from the fully polarized FM Nagaoka regime. This finding is possibly related to the geometrical/topological features of the honeycomb lattice, as pointed out in [53]. In particular, for the honeycomb lattice Ref. [53] reported the tendency for the Nagaoka state in several disconnected regions of the phase diagram. The number of loops on the lattice and some properties of its density of states (such as the quasigap and logarithmic divergence of the Van Hove singularity, as in the present work), which govern the electronic behavior in an unexpected manner in the hole-doped regime, are essential for the Nagaoka mechanism. For the honeycomb lattice, these features could yield a FM ground state after the energetically favorable AFM ground state in the large-U context of the low hole-doped regime. We further mention a quite recent work [54] that has also found this trend for competition between the AFM and FM phases on the honeycomb lattice, even for low hole doping and electronic interactions away from the infinite U limit (Nagaoka mechanism).

It is also worth noticing that the above sequence of ground-state energies keeps unaltered in the strong-coupling regime with $J/t \ll 1$, as depicted in the inset of Fig. 3. Notwithstanding, in the $J = 0$ (infinite-U) limit the mentioned ground states become degenerate. We stress, however, that due to Nagaoka's theorem [55] the infinite-U ground state with a single hole should display long-range FM order with fully polarized spins in the thermodynamic limit (Nagaoka state).

We also mention the very recent work [54] that found, for $\delta = 0.02$ and $J/t = 0.05$, the GTPS numerical $E/Nt \approx -0.10$, in good agreement with our finding, $E/Nt \approx -0.13$ (see inset of Fig. 3).

We now turn to the analysis of the high hole-doped regime. Figure 4 is the counterpart of Fig. 3, but for high hole doping away from half filling. Indeed, the value of the chemical potential in Fig. 4, $\mu/t = -1$, corresponds to hole densities in the vicinity of the Van Hove singularity near the critical doping δ_c. A remarkable switch of position in the ground-state energy curves is noticed, in comparison with the low-doped regime in Fig. 3. The results indicate a dominant chiral $d_1 + id_2$-wave superconducting order with the lowest ground-state energy (pink circles). This finding is in agreement with previous studies in the weak-coupling [19] and strong-coupling [20,36–40] regimes of a variety of systems with honeycomb lattice structure displaying chiral superconductivity.

The curve associated with the s-wave state comes next in Fig. 4 (green triangles up), however with a ground-state energy undisputedly larger than that of the chiral superconducting state in the interval $0.1 \lesssim J/t \leqslant 1$. We also note that the doped AFM state has energy at $T = 0$ lower than the doped FM one. Moreover, just as in the inset of Fig. 3, the inset of Fig. 4 shows the degeneracy in the $J/t = 0$ (infinite-U) limit.

At this point, it is worth mentioning that the results of Figs. 3 and 4 unveiled features embedded in the electronic spectrum $E_{\boldsymbol{k}}^{SC}$ of the $d_{x^2-y^2}$- and d_{xy}-wave states, Eq. (12), plotted in Figs. 5(a) and 5(b). It is interesting to note that the lower (green) and upper (blue) bands collapse in a flat (red) band ($E_{\boldsymbol{k}}^{SC} = 0$) at the critical temperature T_c of each symmetry, Eq. (28). In fact, flat bands may emerge in fermionic systems with diverging density of states (Van Hove singularity) [56]. This feature is also present in the superconducting chiral $d_1 + id_2$-wave state.

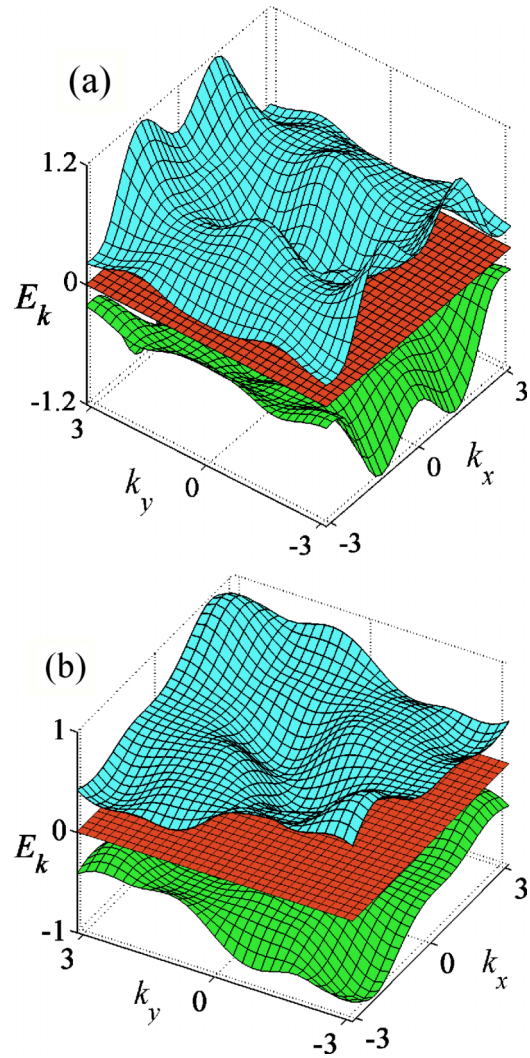

FIG. 5. Energy spectrum, $E_{\boldsymbol{k}}^{SC}$, of the (a) $d_{x^2-y^2}$- and (b) d_{xy}-wave superconducting phases for $J/t = 1/3$ and $\mu/t = -1$, in the vicinity of the Van Hove singularity of the high hole-doped regime near δ_c. At the critical temperature of each symmetry, the lower (green) and upper (blue) bands collapse in a flat (red) band, $E_{\boldsymbol{k}}^{SC} = 0$.

First-order transition and phase separation

The above results indicate that the doped AFM and chiral superconducting ground states are in direct competition with each other, with the former (latter) prevailing in the low (high) hole-doped regime.

To deepen the understanding of this scenario, we plot in Fig. 6(a) the staggered magnetization m as a function of the hole density δ, for $J/t = 1/3$ and $T = 0$. At half filling ($\delta = 0$), the presence of the long-range AFM order yields the maximum $m = 1/2$, which corresponds to the Néel state on the honeycomb lattice. For higher δ, the doped AFM regime displays a monotonically decreasing m, up to the hole density $\delta_{\mathrm{AFM}} \approx 0.15$ at which m nullifies, settling the breakdown of

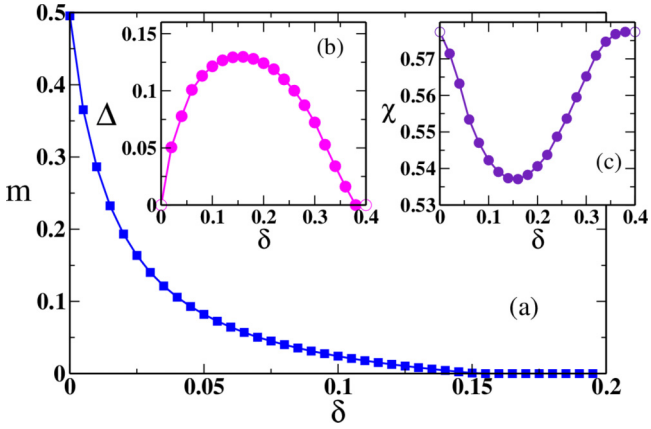

FIG. 6. (a) Staggered magnetization m as a function of the hole doping δ, for $J/t = 1/3$ and $T = 0$. At half filling ($\delta = 0$), the maximum $m = 1/2$ corresponds to the long-range AFM order (Néel state). For higher δ, m decreases monotonically and nullifies at $\delta_{\mathrm{AFM}} \approx 0.15$, where the short-range AFM order breaks down. This value remarkably coincides with the optimal doping, $\delta_{\mathrm{opt}} \approx 0.15$, at which the pairing Δ and hopping χ components of the chiral $d_1 + id_2$-wave superconducting order parameter are maximum and minimum, respectively [insets (b) and (c)].

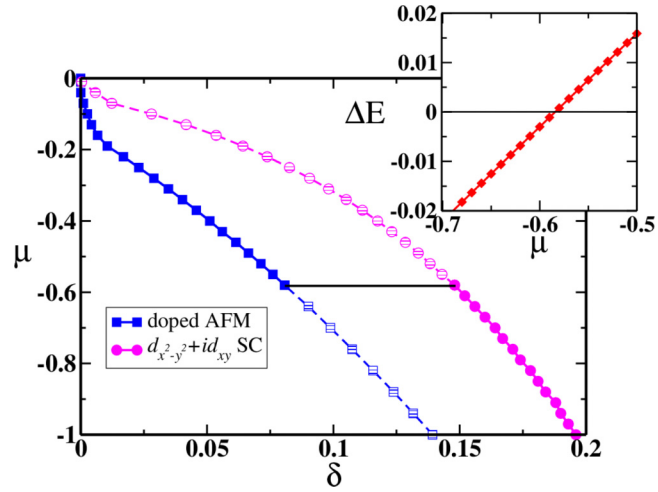

FIG. 7. Chemical potential μ for the doped AFM (blue squares) and chiral $d_1 + id_2$-wave superconducting (pink circles) states as a function of the hole doping δ, for $J/t = 1/3$ and $T = 0$. The inset shows the ground-state energy difference ΔE between these phases, with the critical value $\mu_c/t \approx -0.58$ for $\Delta E = 0$ setting the boundary between the lowest ground-state energy of the doped AFM ($\Delta E < 0, \mu < \mu_c$) and chiral superconducting ($\Delta E > 0, \mu > \mu_c$) phases. The horizontal black line in the main plot indicates the phase separation regime in this first-order transition (Maxwell construction).

the short-range AFM order away from half filling. This value remarkably coincides with the optimal doping, $\delta_{\mathrm{opt}} \approx 0.15$, at which the pairing component Δ of the chiral $d_1 + id_2$-wave superconducting order parameter is maximum, for the same set of parameters. For completeness, in the insets of Fig. 6 we have also included the pairing and hopping components of the superconducting order parameters. We further notice that this value of δ_{AFM} is also in good agreement with previous reports [21,23] on the honeycomb lattice, and with a very recent GTPS result [54] for $t/J = 3$ and $D = 14$, which shows the collapse of the AFM phase located in the range $0.12 < \delta \leqslant 0.15$.

These findings open the possibility of a quantum first-order transition with coexistence at $T = 0$ of both doped AFM and chiral superconducting phases with spatial phase separation. Indeed, Fig. 7 shows the chemical potential μ of the doped AFM (blue squares) and chiral superconducting (pink circles) phases as a function of δ, for $J/t = 1/3$ and $T = 0$. The inset displays the (normalized) ground-state energy difference between these states,

$$\Delta E = \frac{(E_{d_1+id_2} - E_{\mathrm{AFM}})}{Nt}, \tag{34}$$

with the energy expressions given in Eqs. (26) and (32). We notice that the critical value $\mu_c/t \approx -0.58$ at $T = 0$, for which $\Delta E = 0$, sets the boundary between the lowest ground-state energy of the doped AFM ($\Delta E < 0, \mu < \mu_c$) and chiral superconducting ($\Delta E > 0, \mu > \mu_c$) phases. For $\mu = \mu_c$ the system at $T = 0$ jumps from the doped AFM order to the chiral $d_1 + id_2$-wave superconducting state in a first-order transition, which indicates that there exists a window of forbidden doping densities and unstable states described by a Maxwell construction (black horizontal line connecting the μ curves in the main plot of Fig. 7) in the phase separation region. In fact, it can be shown in the context of a Hubbard model with strong Coulomb repulsion that this window of forbidden densities in the phase separation phenomenon is closely related to a wrong energy convexity and/or negative compressibility; see, e.g., Refs. [57–59].

IV. CONCLUSIONS

The importance of advancing the understanding of the superconducting phase in systems with honeycomb/hexagonal crystalline structure can be hardly overstated. Indeed, several compounds with the honeycomb lattice, including the graphene monolayer nanostructure, have been reported to display chiral superconductivity.

Here we have investigated the competition between the superconducting and magnetic phases on a system described by the Hubbard model on the honeycomb lattice, as a function of the electronic coupling and hole-doping density. We have built, in a functional integral approach, a low-energy perturbative theory for the strong-coupling limit of the Hubbard Hamiltonian, both at half filling and in the low and high hole-doped regimes. The effective low-lying Hamiltonian has been expressed in terms of charge (Grassmann fields) and spin [SU(2) gauge fields] degrees of freedom. In particular, by calculating the ground-state energy, electronic spectrum, and other observables associated with the s- and $d_{x^2-y^2} + id_{xy}$-wave superconducting phases, doped antiferromagnetic, and doped ferromagnetic states, we have found that the antiferromagnetic order has the lowest ground-state energy for low hole doping near half filling. On the other hand, a dominant superconducting state with chiral $d_{x^2-y^2} + id_{xy}$-wave symmetry emerges in the vicinity of the Van Hove singularity (high hole doping). A first-order transition with coexistence of these

states takes place along with spatial phase separation, characterized by a Maxwell construction in the plot of the chemical potential versus hole-doping density.

We hope our findings can stimulate further theoretical progress and experimental advances on doped and undoped compounds presenting competing magnetic and chiral superconducting phases, especially those displaying honeycomb or hexagonal lattice structure.

ACKNOWLEDGMENTS

F.G.R. thanks the Agreste Academic Center of the Universidade Federal de Pernambuco (UFPE), in Caruaru, for providing the working conditions to conduct the present investigations. F.G.R. also thanks the Graduate Program in Physics of UFPE, in Recife. We acknowledge the support from the Brazilian agencies Coordenação de Aperfeiçoamento de Pessoal de Nível Superior (CAPES), PROEX 534/2018, No. 23038.003382/2018-39; and Fundação de Amparo à Ciência e Tecnologia do Estado de Pernambuco (FACEPE), research grant PRONEX Program funded by CNPq and FACEPE, APQ-0602-1.05/14. M.D.C.-F. and E.P.R. fellowship grants 304646/2019-9 and 305062/2017-4, respectively, from Conselho Nacional de Desenvolvimento Científico e Tecnológico (CNPq).

APPENDIX: ELECTRONIC DENSITY OF STATES AND VAN HOVE SINGULARITY

Here we calculate the electronic density of states in the noninteracting tight-binding case ($U = 0$), in order to investigate its structure near the K and M points, respectively associated with the Dirac points at the bands intersection and Van Hove singularity.

We start by writing the density of states with energy (in t units) between ε and $\varepsilon + d\varepsilon$, per unit cell and in the thermodynamic limit, as

$$\rho(\varepsilon) = \lim_{N_c\to\infty} \frac{1}{N_c} \sum_{\boldsymbol{k}\sigma} \delta_{\varepsilon,\epsilon_{\boldsymbol{k}}/t}, \tag{A1}$$

where $\epsilon_{\boldsymbol{k}}$ is given in Eq. (13). By taking the continuous limit of the first BZ sums in k_x and k_y, we find $\rho(\varepsilon) = 2|\varepsilon| g(\varepsilon^2)$, where, after suitable changes of variables, we define the distribution function:

$$g(\varepsilon^2) = \frac{1}{\pi^2} \int_0^\pi d\theta \int_0^\pi d\phi\, \delta(\varepsilon^2 - 1 - 4\cos(2\theta)\cos(\phi) - 4\cos^2(2\theta)). \tag{A2}$$

Further substitutions, $u = \cos(2\theta)$ and $\upsilon = \cos(\phi)$, yield

$$g(\varepsilon^2) = \frac{2}{\pi^2} \int_{-1}^{1} du \int_{-1}^{1} d\upsilon \frac{\delta(\varepsilon^2 - 1 - 4u\upsilon - 4u^2)}{2\sqrt{1-u^2}\sqrt{1-\upsilon^2}}. \tag{A3}$$

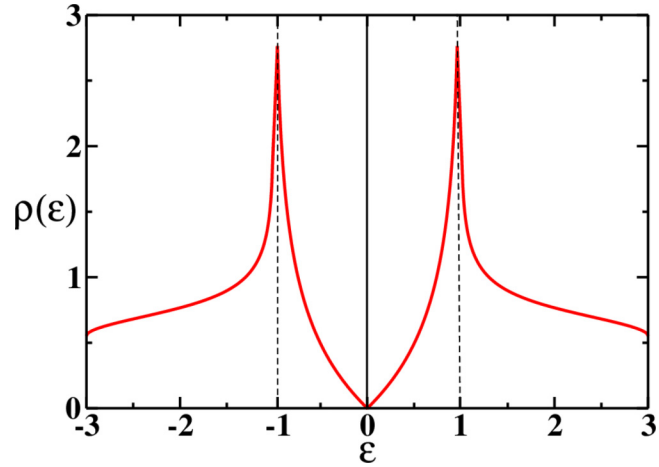

FIG. 8. Density of states per unit cell, $\rho(\varepsilon)$, as a function of the energy ε (in t units) for the noninteracting tight-binding case. The energy origin was chosen at the $K_\pm$ Dirac points at which ρ nullifies. Van Hove logarithmic singularities take place at $\varepsilon = \pm 1$.

Next, by considering the complete elliptical integral of the first kind [42], $\mathbb{F}(\pi/2, x)$, so that

$$\int_\alpha^\beta \frac{dx}{x(\gamma - x)(\beta - x)(\alpha - x)} = A\,\mathbb{F}\left(\frac{\pi}{2}, \sqrt{\frac{\alpha(\beta-\gamma)}{\beta(\alpha-\gamma)}}\right), \tag{A4}$$

with $A = 2/\sqrt{\beta(\alpha-\gamma)}$ and $\alpha \geqslant \beta \geqslant \gamma \geqslant 0$, we finally obtain

$$\rho(\varepsilon) = \frac{4|\varepsilon|}{\pi^2 t^2 \sqrt{Z_0}} \mathbb{F}\left(\frac{\pi}{2}, \sqrt{\frac{Z_0}{Z_1}}\right), \tag{A5}$$

in which

$$Z_0 = \begin{cases} (1+|\varepsilon|)^2 - \frac{1}{4}(|\varepsilon|^2 - 1)^2, & \text{for } |\varepsilon| \leqslant 1, \\ 4|\varepsilon|, & \text{for } 1 \leqslant |\varepsilon| \leqslant 3, \end{cases} \tag{A6}$$

and

$$Z_1 = \begin{cases} 4|\varepsilon|, & \text{for } |\varepsilon| \leqslant 1, \\ (1+|\varepsilon|)^2 - \frac{1}{4}(|\varepsilon|^2 - 1)^2, & \text{for } 1 \leqslant |\varepsilon| \leqslant 3. \end{cases} \tag{A7}$$

Figure 8 displays $\rho(\varepsilon)$ with the energy origin (neutrality point $\varepsilon = 0$) chosen at the $K_\pm$ Dirac points, around which it vanishes linearly, $\rho(\varepsilon) \approx 2|\varepsilon|/(\pi\sqrt{3})$, $|\varepsilon| \ll 1$. On the other hand, we note that the density of states presents a logarithmic divergence at the Van Hove singularities (M points with $|\varepsilon| = 1$).

Therefore, by properly tuning the chemical potential under hole-doping the system, one can move from the K points to the M points of the first Brillouin zone, at which the density of states presents logarithmic divergence in the high hole-doped regime (Van Hove singularity).

[1] P. W. Anderson, *The Theory of Superconductivity in the High-T_c Cuprate Superconductors* (Princeton University Press, Princeton, 1997).

[2] P. W. Anderson, Science **177**, 393 (1972).

[3] R. Combescot, *Superconductivity* (Cambridge University Press, Cambridge, 2022).

[4] S. J. Blundell, *Superconductivity: A Very Short Introduction* (Oxford University Press, Oxford, 2009).

[5] L.-P. Lévy, *Magnetism and Superconductivity* (Springer, Berlin, 2000).

[6] L. K. Tran (ed.), *Superconductivity, Magnetism and Magnets* (Nova Science Publishers, New York, 2006).

[7] A. V. Chubukov and P. J. Hirschfeld, Phys. Today **68**(6), 46 (2015).

[8] W. Nolting and A. Ramakanth, *Quantum Theory of Magnetism* (Springer, Berlin, 2010).

[9] U. Schollwöck, J. Richter, D. J. J. Farnell, and R. F. Bishop (eds.), *Quantum Magnetism* (Springer, Berlin, 2004).

[10] A. Auerbach, *Interacting Electrons and Quantum Magnetism* (Springer, New York, 1994).

[11] Y. J. Yan, Z. Y. Li, T. Zhang, X. G. Luo, G. J. Ye, Z. J. Xiang, P. Cheng, L. J. Zou, and X. H. Chen, Phys. Rev. B **85**, 085102 (2012).

[12] A. Möller, U. Löw, T. Taetz, M. Kriener, G. André, F. Damay, O. Heyer, M. Braden, and J. A. Mydosh, Phys. Rev. B **78**, 024420 (2008).

[13] V. Kataev, A. Möller, U. Löw, W. Jung, N. Schittner, M. Kriener, and A. Freimuth, J. Magn. Magn. Mater. **290**, 310 (2005).

[14] Y. Miura, R. Hirai, Y. Kobayashi, and M. Sato, J. Phys. Soc. Jpn. **75**, 084707 (2006).

[15] S. A. J. Kimber, I. I. Mazin, J. Shen, H. O. Jeschke, S. V. Streltsov, D. N. Argyriou, R. Valentí, and D. I. Khomskii, Phys. Rev. B **89**, 081408(R) (2014).

[16] S. J. Youn, M. H. Fischer, S. H. Rhim, M. Sigrist, and D. F. Agterberg, Phys. Rev. B **85**, 220505(R) (2012).

[17] P. K. Biswas, H. Luetkens, T. Neupert, T. Stürzer, C. Baines, G. Pascua, A. P. Schnyder, M. H. Fischer, J. Goryo, M. R. Lees, H. Maeter, F. Brückner, H.-H. Klauss, M. Nicklas, P. J. Baker, A. D. Hillier, M. Sigrist, A. Amato, and D. Johrendt, Phys. Rev. B **87**, 180503(R) (2013).

[18] L.-F. Zhang, Y.-Y. Zhang, G.-Q. Zha, M. V. Milosević, and S.-P. Zhou, Phys. Rev. B **101**, 064501 (2020).

[19] R. Nandkishore, L. S. Levitov, and A. V. Chubukov, Nat. Phys. **8**, 158 (2012).

[20] W. Wu, M. M. Scherer, C. Honerkamp, and K. Le Hur, Phys. Rev. B **87**, 094521 (2013).

[21] Z. C. Gu, H. C. Jiang, D. N. Sheng, H. Yao, L. Balents, and X. G. Wen, Phys. Rev. B **88**, 155112 (2013).

[22] Y. Vielza, A. C. M. de Oca, M. D. Coutinho-Filho, and E. P. Raposo, Eur. Phys. J. B **95**, 33 (2022).

[23] F. G. Ribeiro and M. D. Coutinho-Filho, Phys. Rev. B **92**, 045105 (2015).

[24] A. H. Castro Neto, F. Guinea, N. M. R. Peres, K. S. Novoselov, and A. K. Geim, Rev. Mod. Phys. **81**, 109 (2009).

[25] V. N. Kotov, B. Uchoa, V. M. Pereira, F. Guinea, and A. H. Castro Neto, Rev. Mod. Phys. **84**, 1067 (2012).

[26] J. W. Negele and H. Orland, *Quantum Many-Particle Systems* (CRC Press, Boca Raton, 1998).

[27] E. Fradkin, *Field Theories of Condensed Matter Systems* (Cambridge University Press, Cambridge, 2013).

[28] X. G. Wen, *Quantum Field Theory of Many-Body Systems* (Oxford University Press, Oxford, 2010).

[29] A. Altland and B. Simons, *Condensed Matter Field Theory* (Cambridge University Press, Cambridge, 2010).

[30] Z. Y. Weng, D. N. Sheng, C. S. Ting, and Z. B. Su, Phys. Rev. Lett. **67**, 3318 (1991).

[31] Z. Y. Weng, D. N. Sheng, C. S. Ting, and Z. B. Su, Phys. Rev. B **45**, 7850 (1992).

[32] M. H. Oliveira, E. P. Raposo, and M. D. Coutinho-Filho, Phys. Rev. B **80**, 205119 (2009).

[33] M. Z. Hasan and C. L. Kane, Rev. Mod. Phys. **82**, 3045 (2010).

[34] E. P. Raposo and M. D. Coutinho-Filho, Phys. Rev. Lett. **78**, 4853 (1997); **79**, 2754(E) (1997).

[35] E. P. Raposo and M. D. Coutinho-Filho, Phys. Rev. B **59**, 14384 (1999).

[36] A. M. Black-Schaffer, W. Wu, and K. Le Hur, Phys. Rev. B **90**, 054521 (2014).

[37] A. M. Black-Schaffer, Phys. Rev. Lett. **109**, 197001 (2012).

[38] J. Linder, A. M. Black-Schaffer, T. Yokoyama, S. Doniach. and A. Sudbo, Phys. Rev. B **80**, 094522 (2009).

[39] A. M. Black-Schaffer and S. Doniach, Phys. Rev. B **75**, 134512 (2007).

[40] J. Vučičević, M. O. Goerbig, and M. V. Milovanović, Phys. Rev. B **86**, 214505 (2012).

[41] P. A. Lee, N. Nagaosa, and X. G. Wen, Rev. Mod. Phys. **78**, 17 (2006).

[42] H. Scher and R. Zallen, J. Chem. Phys. **53**, 3759 (1970).

[43] T. Watanabe and S. Ishihara, J. Phys. Soc. Jpn. **82**, 034704 (2013).

[44] J. L. McChesney, A. Bostwick, T. Ohta, T. Seyller, K. Horn, J. González, and E. Rotenberg, Phys. Rev. Lett. **104**, 136803 (2010).

[45] I. S. Gradshteyn and I. M. Ryzhik, *Tables of Series, Products and Integrals* (Elsevier, Amsterdam, 2007).

[46] J. D. Reger, J. A. Riera, and A. P. Young, J. Phys.: Condens. Matter **1**, 1855 (1989).

[47] U. Löw, Condens. Matter Phys. **12**, 497 (2009).

[48] W. Zheng, J. Oitmaa, and C. J. Hamer, Phys. Rev. B **44**, 11869 (1991).

[49] J. Oitmaa, C. J. Hamer, and W. Zheng, Phys. Rev. B **45**, 9834 (1992).

[50] H. C. Jiang, Z. Y. Weng, and T. Xiang, Phys. Rev. Lett. **101**, 090603 (2008).

[51] Z. Y. Xie, H. C. Jiang, Q. N. Chen, Z. Y. Weng, and T. Xiang, Phys. Rev. Lett. **103**, 160601 (2009).

[52] H. H. Zhao, Z. Y. Xie, Q. N. Chen, Z. C. Wei, J. W. Cai, and T. Xiang, Phys. Rev. B **81**, 174411 (2010).

[53] T. Hanisch, B. Kleine, A. Ritzl, and E. Müller-Hartmann, Ann. Phys. **507**, 303 (1995).

[54] J.-J. Miao, Z.-Y. Yue, H. Zhang, W.-Q. Chen, and Z.-C. Gu, arXiv:2301.02274.

[55] Y. Nagaoka, Phys. Rev. **147**, 392 (1966).

[56] N. B. Kopnin, T. T. Heikkilä, and G. E. Volovik, Phys. Rev. B **83**, 220503(R) (2011).

[57] A. M. S. Macêdo, M. C. dos Santos, M. D. Coutinho-Filho, and C. A. Macêdo, Phys. Rev. Lett. **74**, 1851 (1995).

[58] R. R. Montenegro-Filho and M. D. Coutinho-Filho, Phys. Rev. B **74**, 125117 (2006).

[59] M. Capone and G. Kotliar, Phys. Rev. B **74**, 054513 (2006).